Investigation of High-Lift Flowfield of an Energy Efficient Transport Wing

Mert E. Berkman,* Mehdi R. Khorrami,† Meelan Choudhari,‡ and Shelly S. Sadowski§
High Technology Corporation, Hampton, Virginia 23666

The high-lift flowfield around a multielement energy efficient transport wing is investigated both experimentally and numerically. Special emphasis is placed on resolving aeroacoustically relevant local features of the mean flowfield, e.g., separated flow regions including recirculation bubbles, free shear layers/wakes/jets, and vortices. Such features are typically present in slat and flap cove areas, flap side-edge regions, and slat-main-wing confluent boundary layer. The flow fluctuations sustained in these regions can generate significant noise, especially via interaction with nearby airframe structures. The experimental measurements and computed results presented here show excellent agreement for mean aerodynamic quantities and provide valuable physical insight into potential sources of flow unsteadiness, such as the vortex system near the flap side edge. Whereas the generic features of the computed flowfield are similar to other published studies, the specific details of the acoustically relevant flow features are found to depend on the geometry of the high-lift configuration.

Nomenclature

C_p	=	pressure coefficient
c	=	stowed chord length
g_f	=	flap gap
g_s	=	slat gap
M	=	Mach number
o_f	=	flap overlap
o_s	=	slat overlap
Re	=	Reynolds number based on stowed chord
u	=	streamwise velocity component
x, y, z	=	streamwise, normal, and spanwise directions
α	=	angle of attack
δ_f	=	flap deflection angle
δ_s	=	slat deflection angle

I. Introduction

THE objective of this paper is to investigate the localized flow-field features of a high-lift system that are potentially important in the generation of nonpropulsive, i.e., airframe noise by an aircraft. As a consequence of both the continued success in reducing engine noise and the increasingly stringent aircraft noise regulations, airframe noise has emerged as an important component of the overall aircraft noise acoustic emissions. Particularly during landing, when an aircraft operates at a low-power setting, airframe becomes the major noise source. Therefore, following an active phase of research during the 1970s,[1] prediction and abatement of airframe noise has witnessed a recent resurgence of interest on both sides of the Atlantic.[2,3] The dominant sources of airframe noise in subsonic aircraft are connected with aerodynamic unsteadiness related to the high-lift system and the landing gear.[1] However, the geometric and aerodynamic complexity of these systems has eluded a fundamental understanding (and, hence, control) of the associated noise sources. Consequently, the existing prediction techniques for airframe noise (as embodied, for instance, by the Fink model[4] in NASA's Aircraft Noise Prediction Program) use semi-empirical curve fitting based on rather limited knowledge of the actual noise sources. More importantly, however, the preceding techniques fail to describe some of the causal dependencies that are vital for effective abatement of airframe noise radiation.

NASA's Advanced Subsonic Technology–Noise Reduction Program, which began in 1994, seeks to correct the latter deficiency by developing a second-generation prediction scheme that incorporates a tighter coupling between the far-field noise and the fundamental fluid mechanics of the unsteady near-field disturbances.[2] Toward this development, the NASA program has launched a systematic investigation involving a synergistic set of building-block experiments[5,6] and computations[7−12] that span the entire cause-effect chain related to airframe noise. The first set of experiments were carried out in the NASA Ames 7 × 10 ft Wind Tunnel[5] and the Langley Quiet Flow Facility (QFF).[6] Both experiments involved an unswept constant chord wing with a partial-span flap under approach conditions, and the flap side edge was identified as a major noise source as expected. The accompanying computations involved a three step sequence of 1) mean-flow computations based on Reynolds-averaged Navier–Stokes (RANS) equations,[7−9] 2) unsteady flow calculations modeling the large-scale coherent structures supported by the mean flow,[11,12] and 3) prediction of radiated noise based on some form of acoustic analogy.[12] In addition to accurately reproducing a number of experimentally observed features of both flow and acoustics, the preceding studies clearly showed the dominant source of flap noise to be associated with the formation of the flap side-edge vortex system.

The next set of airframe noise experiments was carried out in NASA Langley's Low Turbulence Pressure Tunnel (LTPT). These tests were aimed at determining the velocity scaling laws for flap and slat noise, especially in a Reynolds-number range approaching flight values. Similar to the 7 × 10 and QFF tests, the model tested had an unswept geometry, with a part-span flap and full-span slat; however, unlike the prior tests, the wing section tested in LTPT was representative of a generic energy efficient transport (EET). Extensive aerodynamic and acoustic measurements were conducted during the test. This paper reports on the aerodynamic investigation of the EET flowfield under approach conditions.

A brief overview of the experiment and accompanying RANS calculations is given in Secs. II.A–II.C. The computed solutions are compared with the measured on-surface data in Sec. III. During the computational procedure, special attention was given to the regions where significant flow noise generation is expected, namely, the flap side edge, slat and flap cove regions, and the confluent boundary layer over the upper surface of the main element. By revealing

*Research Scientist. Member AIAA.

†Senior Scientist. Senior Member AIAA.

‡Senior Research Scientist; currently Research Scientist, NASA Langley Research Center, Hampton, VA 23681. Senior Member AIAA.

§Research Scientist; currently Training Engineer, Shiller Service Corporation, 1001 Thomas Street, Hampton, VA 23669. Senior Member AIAA.

such additional details of the flowfield that might not otherwise be available, the RANS simulations can uncover potential sources of near-field unsteadiness and, hence, yield important physical insights into the nature of airframe noise sources and as to how these sources may vary from configuration to configuration. The highly resolved flowfield presented herein will subsequently serve as a basis for acoustic modeling, along the same lines as the previous studies of flap side-edge noise.[8,11,12]

II.   Experimental and Numerical Procedure

A.   Experiment

NASA Langley's LTPT is a closed-circuit pressure tunnel, with independent control of total pressure and flow velocity. Flow temperature may be maintained below a set threshold using cooling vanes. Designed for testing two-dimensional airfoil sections, the test section is 3 ft wide × 7.5 ft tall × 7.5 ft long, and model endplate suction is available for boundary-layer control.

Test conditions for the experiments reported here include free-stream Reynolds numbers (based on stowed chord) of 3.6, 7.2, 14.4, and 19.2 million and Mach numbers of 0.125, 0.2, and 0.3. All of the tests included steady and unsteady surface pressure measurements using surface-pressure taps and kulites, respectively. Acoustic measurements were carried out using a phased microphone array mounted on the ceiling. During the initial flap-edge noise test, pressures were mapped in the vicinity of the flap side edge using pressure sensitive paint (PSP). Prior to that entry, two-dimensional laser velocimetry measurements were conducted in the flap side-edge region. Because of acoustic concerns, tunnel side-wall boundary-layer suction was not used for any of these tests. For all acoustic measurements temperature was controlled by tunnel cooling vanes, but automatic control of tunnel pressurization was disabled to avoid noise introduced by control valves.

B.   Model Geometry and Grid Development

The generic EET model in its full configuration is a three-element high-lift system without sweep or taper. The system is comprised of a main element, a leading-edge slat, and a part-span flap as shown in Fig. 1. In stowed position the model has a chord of 21.65 in. (0.55 m) and a span of 36 in. (0.914 m), corresponding to an aspect ratio of 1.66. The slat and flap chords account for 15 and 30%, respectively, of the stowed chord length, and the span of the part-span flap is 19 in. (0.483 m). The relative positions of the slat and the flap with respect to the wing (i.e., the gaps g_s, g_f and the overhangs o_s, o_f) were fixed to match the experimental settings of interest. Because small deviations in positions can significantly alter the flow details,

a) Model geometry

b) Cross-sectional view

Fig. 1   Three-element EET model.

Table 1   Geometrical settings

Setting	Case 1	Case 2	Case 3
Angle of attack, α	5 deg	5 deg	10 deg
Flap angle, δ_f	20 deg	30 deg	30 deg
Slat angle, δ_s	No slat	No slat	30 deg
Flap gap, g_f	3.0%	3.0%	3.0%
Flap overhang, o_f	1.7%	1.7%	1.7%
Slat gap, g_s	No slat	No slat	2.44%
Slat overhang, o_s	No slat	No slat	−1.52%

extreme care was taken during the grid generation process to match exactly the experimental gap and overhang settings.

Except for a modified flap section, the cross section of the EET model (Fig. 1b) is identical to that of the two-dimensional model described by Lin and Dominik.[13] All of the trailing edges of the tested model are blunt. However, to simplify the computational task and to reduce the overall number of grid points, the top surfaces of respective elements were shaved off smoothly to produce sharp trailing edges. A two-dimensional study was conducted to investigate the effect of sharpening the slat trailing edge, and the results indicated minimal differences between the two for steady-state analysis.

For a realistic comparison with the measured quantities, the entire test section of LTPT was modeled in the computations. However, to avoid excessive computational costs, the wind-tunnel walls were treated as inviscid surfaces. The latter assumption has been shown to be adequate in previous studies of high-lift configurations.[7,8]

Three different configurations were simulated computationally. For all three simulations the normalizing parameters were the stowed chord c, freestream speed of sound, density, and molecular viscosity. The first case involved the wing with the part-span flap (without slat) in an approach setting. The wing was at an angle of attack of 5 deg and the flap deflection δ_f was set at 20 deg. The flap deflection was increased to 30 deg in the second case. The third configuration included the leading-edge slat, deflected at 30 deg with respect to the wing, which itself was at 10-deg angle of attack. The flap deflection remained at 30 deg. The relevant geometrical settings for all three cases are tabulated in Table 1, where the distances are given as percentage of the stowed chord. The slat and flap gaps and overhangs are defined as shown in Fig. 1b. In the experiments, slat and flap overhangs were set using blocks machined to match the main-element leading-edge contour and cove, whereas gaps were set by rearranging spacers at the bracket foot. To confirm accurate model rigging after it was set, gaps were measured at several spanwise stations using gauge blocks.

A structured multiblock grid topology was used to simulate the flow past the multielement configuration. The need for accurate resolution of flap side-edge flowfield and slat cove area increased the number of nodes significantly. A dominant portion of the spanwise grid was clustered so as to resolve the side-edge vortices. Chordwise resolution was also high over the flap, involving 79 (case 3) or 97 (cases 1 and 2) points from leading to trailing edge. Another region of high grid density was the cove of the slat, where a good understanding of the separated flow is required. Several patched block interfaces were used to avoid propagation of these fine grids to the far field.

For the two-element configuration a nine-block grid with approximately 4.8 million nodes was used. The flap side-edge flowfield was finely resolved in the spanwise direction by clustering most of the 145 spanwise nodes in that region. The inclusion of the slat in case 3 demanded further partitioning of the flowfield, resulting in a grid with 16 zones and 5.7 million grid nodes. Because the main purpose of case 3 was to facilitate the understanding of the slat cove flow, a few points in chordwise and spanwise directions were removed from the flap grid used in cases 1 and 2. Redistribution of these points was done with care so as to achieve a minimal degradation of the solution in the flap side-edge area.

In the normal direction typically 15–30 grid points were packed in the boundary layers surrounding the model solid surfaces, with the first point at 5×10^{-6} chords off the surface. Figure 2a shows a cross-sectional view of the grid for the three-element configuration.
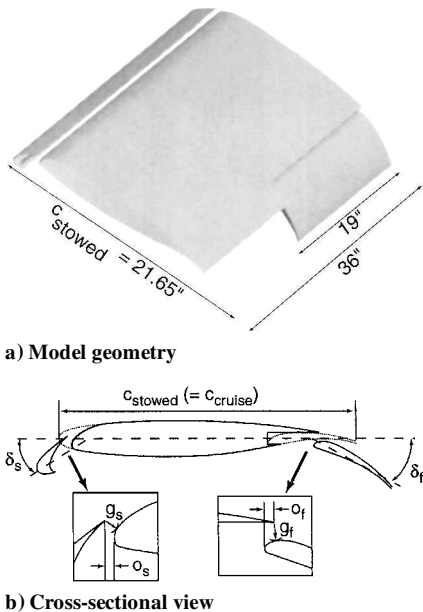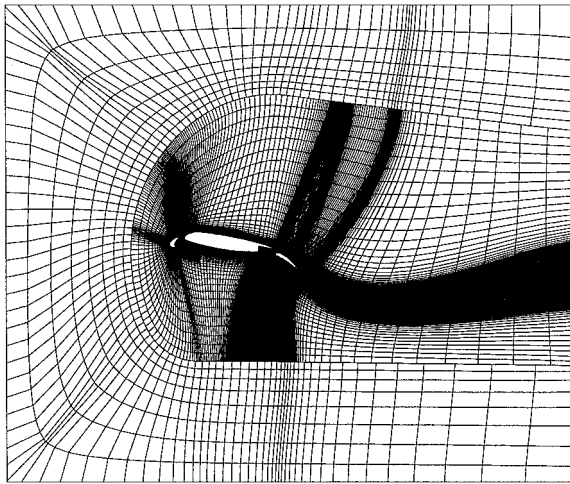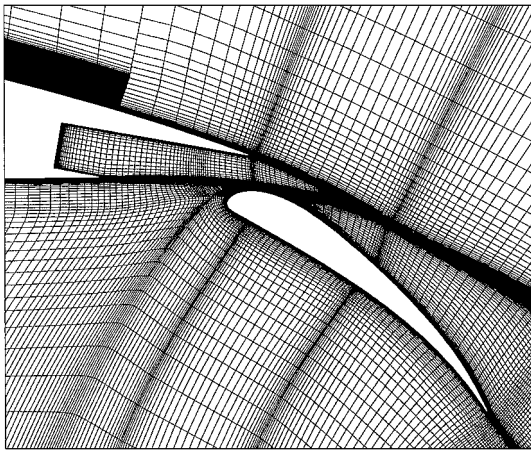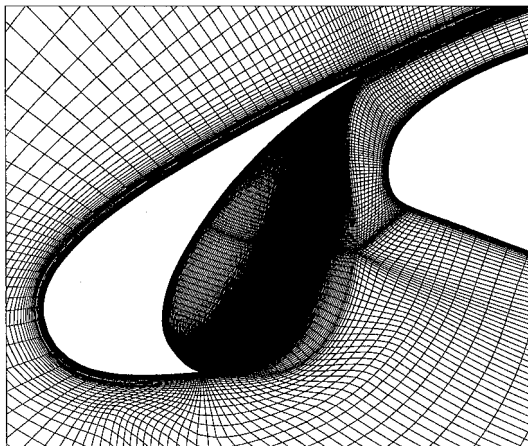
a) Spanwise view

b) Flap region

c) Slat region

Fig. 2 Grid cross section in x–y plane for EET model.

Close-up views of the flap and slat cove regions are shown in Figs. 2b and 2c, respectively.

C. Numerical Scheme

A well-known finite volume flow solver, the CFL3D code[14] developed at NASA Langley Research Center, was used to perform the numerical simulations. The Reynolds-averaged thin-layer Navier–Stokes equations were solved using a globally second-order-accurate spatial discretization. Upwind-biased differencing was used for the inviscid terms, whereas the viscous terms were evaluated using central differencing. In this work Roe-averaged flux-difference splitting was used to approximate the inviscid flux

values at cell faces. CFL3D offers a large number of turbulence models, ranging from zero-equation to two-equation models. All computations presented in this paper are based on the one-equation Spalart–Allmaras model,[15] which had demonstrated as good or better performance than more computationally intensive models in the previous studies[7−9] for similar high-lift configurations. The calculations were performed with the flow assumed to be fully turbulent over the body. The code has provisions for grid sequencing, multi-gridding, and local time stepping to accelerate convergence to steady state. In addition, CFL3D allows non-one-to-one node matching at the block interfaces, i.e., patching, which helps reduce the number of nodes and thus CPU requirements. All of the preceding features were employed in the present simulations to reduce the computational cost.

III. Results and Discussion

In all three cases for which the computations were carried out, the freestream Mach number was set equal to 0.2 and the chord Reynolds number to 7.2 million to match the flow conditions of the nominal experimental run. The preceding combination of parameters represents a typical approach condition. Extensive aerodynamic and acoustic measurements in the LTPT (the Reynolds number was varied between 3.6 and 19.2 million) had revealed that the dominant features of the flowfield were relatively independent of the Reynolds number for values greater that 7 million.

As in any computational study, it is important to provide an estimate of the accuracy of the computed solutions. The convergence to a steady-state solution was assumed when there were no changes in the lift and drag coefficients to five significant digits with subsequent iterations. At this point the overall residual had dropped by 4–5 orders of magnitude relative to its starting value for each case. Understandably, for a three-dimensional geometry of present complexity, only limited grid-resolution studies could be conducted. As just noted, mesh sequencing provided an effective means to obtain a faster convergence rate. Fortunately, it also provides a good estimate (in a global sense) for the grid-size dependency of the solutions. During mesh sequencing, a number of iterations are performed at each grid level starting with the coarsest level. For a three-dimensional grid the resulting coarser mesh (obtained by removing every other node) contains $\frac{1}{8}$ as many nodes as the adjacent higher level grid. Table 2 displays the computed lift coefficient C_L using the mid- and fine-level grids for the three cases studied.

A. Two-Element Configuration

Case 1 involved a two-element configuration comprised of a wing and a part-span flap with the wing at 5 deg of angle of attack and flap deflection of 20 deg. Figure 3 illustrates a comparison of the computed surface pressure coefficient C_p variation with the experimental data at a spanwise distance of 1 in. (0.046 cm) from the flap side edge. Except for minor differences in the vicinity of the flap trailing edge, excellent agreement is observed between the two sets of results. These differences are attributed to the sharpening of the flap trailing edge, which resulted in a slightly increased flap camber in the model geometry used for computations. Further comparison between the computed and measured pressure coefficient contours over the flap side edge and the upper flap surface is shown in Figs. 4 and 5. The experimental results in Fig. 4 are PSP measurements. PSP data presented here have an uncertainty of ±0.07 in pressure coefficient. Again, both sets of data show remarkable agreement, suggesting that all of the important features of the flowfield are being resolved adequately. The finite flap trailing-edge thickness in the actual flap may be observed in Fig. 4b.

Table 2   Grid-resolution studies

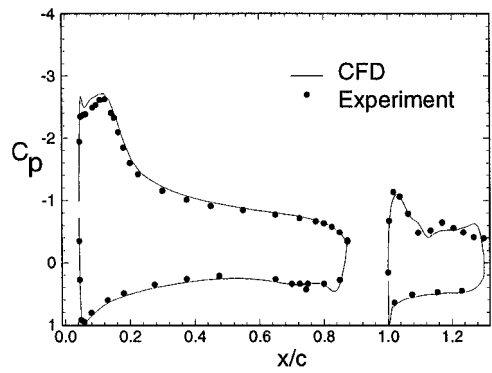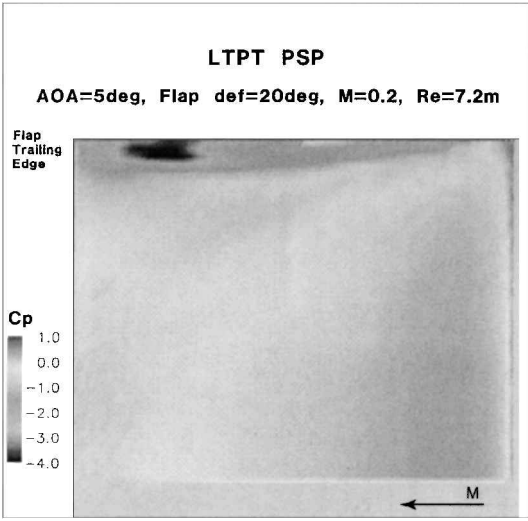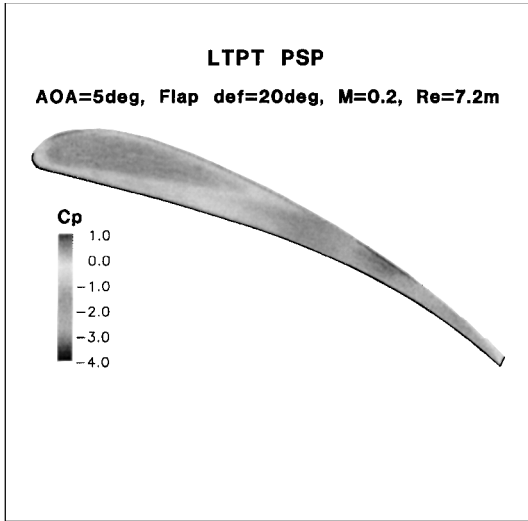|	C_L		
Case	Midlevel mesh	Fine-level mesh	Difference, %
1	1.729	1.714	0.9
2	1.864	1.911	2.46
3	2.348	2.425	3.18

Fig. 3 Chordwise pressure distribution over two-element EET model ($\delta_f = 20$ deg, $M = 0.2$, and $Re = 7.2 \times 10^6$).
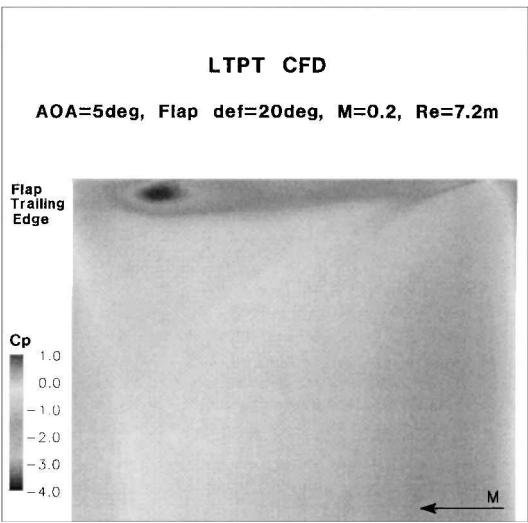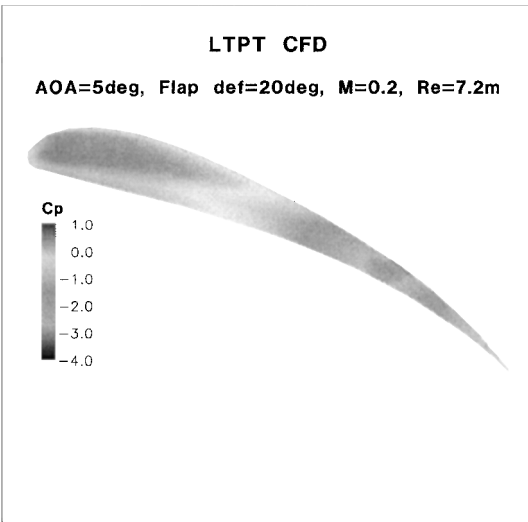

a) Flap top surface

b) Flap side edge

Fig. 4 Measured C_p distribution on flap surface ($\delta_f = 20$ deg, $M = 0.2$, and $Re = 7.2 \times 10^6$).

a) Flap top surface

b) Flap side edge

Fig. 5 Computed C_p distribution on flap surface ($\delta_f = 20$ deg, $M = 0.2$, and $Re = 7.2 \times 10^6$).

Careful flow measurements[5,6] and computational studies[7-9] of the high-lift model tested in 7 × 10 and QFF clearly demonstrated the presence of a dual vortex system at the flap side edge. The EET's surface pressure distribution (Figs. 4 and 5) show the formation of a similar dual vortex system at the flap side edge. Nevertheless, because of a different flap loading in the present case, the relative strength of the vortices and their interaction differs significantly from the previous studies. Here, the stronger of the two vortices

forms on the top surface near the leading edge and moves slightly inboard as it travels towards the flap trailing edge (dark narrow strip in Figs. 4a and 5a). The weaker vortex forms close to the lower sharp corner of the flap side edge where the boundary layer on the flap bottom separates. This vortex, which originates near the flap leading edge, grows both in size and strength in the streamwise direction as indicated by its wedge-shaped footprint and the drop in its core pressure (Figs. 4b and 5b). Experience with acoustic models[11,12] suggests that such differences in vortex characteristics will result in significantly different noise generation.

The evolution of the streamwise vorticity field (contours ranging from −50 to 50) at the flap side edge is presented in a succession of planar cuts along the flap chord in Fig. 6. The chordwise locations of these spanwise planes are highlighted as vertical lines in Fig. 6a. Also displayed in Fig. 6a are the outlines of wing trailing-edge geometry on the flap side (white area only) and no-flap side (white gray area). Note that at the side edge, there is a significant side lap between the flap and the main element, extending over 40% of the flap chord. The ramification of this extensive side-lap region, which is absent in the 7 × 10 configuration,[5] is quite significant. Here, the established flowfield is structurally richer and more complex than the 7 × 10 flowfield.[8]

The streamwise vorticity contours at $x/c = 0.90$ are shown in Fig. 6b. Notice that in addition to the flap vortices, a dual vortex system of opposite sign vorticity is also established at the main
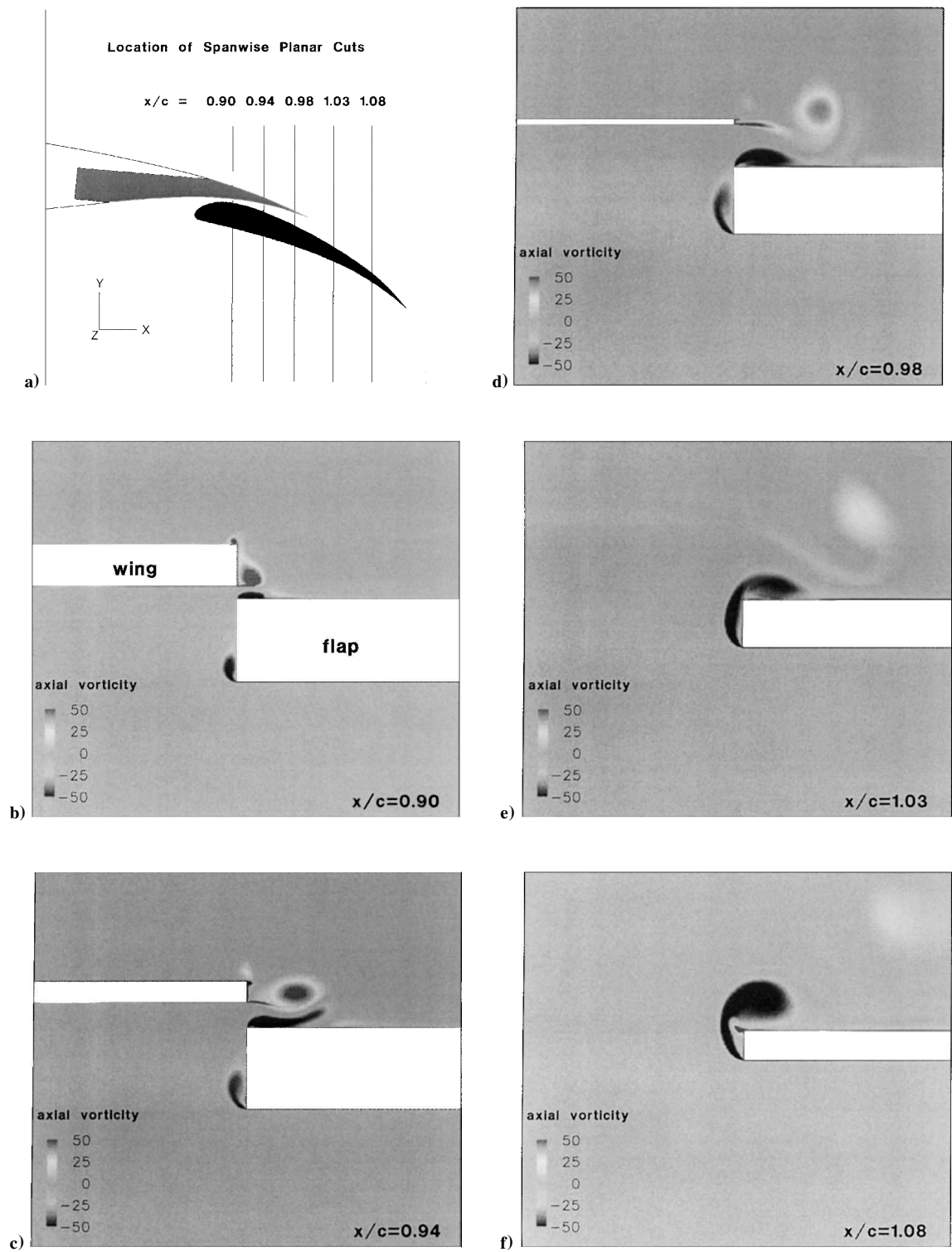
Fig. 6   Axial vorticity contours at flap side edge.

element side edge. Because of the strong spanwise flow through the side-lap region, the vortex on top of the flap is flattened noticeably. At $x/c = 0.94$ (Fig. 6c) the spanwise flow on the main element bottom and top surfaces becomes stronger toward the edge, and in the process it detaches the wing top vortex from the surface, diminishing its strength. At the same time the wing side-edge vortex is pushed away from the edge, severely deforming the flap top vortex while moving laterally. At $x/c = 0.98$ near the wing trailing edge (Fig. 6d), the wing vortex continues its lateral movement, and in the process gets wrapped at its outer edge by a sheath of opposite

sign vorticity. Note that because of boundary-layer separation at the wing bottom edge, a strong free shear layer is formed at the wing side edge, which directly feeds the wing vortex. Similarly formed shear layers at the flap top and bottom sharp edges feed their respective flap vortices. Recent noise source modeling efforts by Khorrami and Singer[11] and Streett[12] strongly suggest that the unsteady perturbations supported by these shear layers and vortices play a dominant role in noise generation at the flap side edges.

Downstream of the side-lap region (Fig. 6e), the wing vortex is moved far enough from the side edge that it no longer interacts with

the flap surface. Furthermore, the vortex is diffused, and its strength is diminished significantly. This excessive diffusion, in our opinion, is primarily numerical but largely inconsequential as described next. Streamwise vortices, once formed, are extremely persistent and seldom become diffused in such a short distance. Unfortunately, in the present case, as the vortex movement gradually displaces it farther and farther away from the flap side edge, it is moving away from the region of highest resolution. However, because the wing vortex resides far from the flap top surface or any of the flap sharp edges, it is not viewed as a dominant noise source. Therefore, a decision was made early on to focus on the flap side edge vortices and not to redistribute the spanwise grid points to better resolve this particular vortex.

Returning to the $x/c = 1.03$ location (Fig. 6e), because of the smaller flap thickness and vortex growth the side vortex is in the process of moving on top and interacting with the flap top vortex. Further downstream at $x/c = 1.08$ (Fig. 6f), the streamwise vorticity field indicates merging and formation of a single vortex on the top surface. However, it is seen that the two side-edge vortices still remain distinct by viewing the velocity field that is not plotted here for brevity. At this station the top vortex is lifted off the surface, creating a strong spanwise flow underneath toward the edge. In comparison to the 7×10 configuration,[8] the top vortex remains closer to the flap upper surface. At the edge the spanwise flow separates and forms a free shear layer of opposite sign vorticity. Also visible is the remnant of the wing vortex at the top right corner of Fig. 6e.

At a streamwise location slightly downstream of $x/c = 1.08$, the flap top vortex can no longer negotiate the strong adverse pressure gradient on the top surface and breaks down. Vortex breakdown in such a high-lift setting was first observed[6] and computed[8] for the 7×10 configuration. The presence of vortex breakdown in the present EET flowfield indicates that the phenomenon is not unique to the 7×10 configuration and very likely is a common feature at high flap deflections. The flow streamlines near the flap side-edge region are shown in Fig. 7. Each streamline represents one of the three major vortices present. The figure provides a good global view of the location of the vortices, as well as the vortex interaction, merging, and breakdown processes. Contrary to the 7×10 configuration, where the merging of the flap vortices occurred ahead of the breakdown, here the side vortex gets wrapped around the top vortex in the breakdown region, and the full merging process takes place downstream of this region.

A streamwise planar cut through the vortex breakdown region slightly inboard of the flap side edge is shown in Fig. 8. These streamlines are restricted to the plane and therefore contain no information with regard to the spanwise flow. The figure shows the
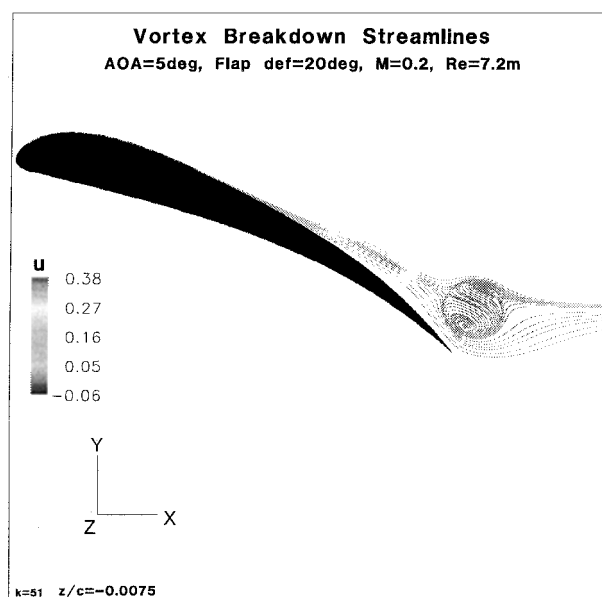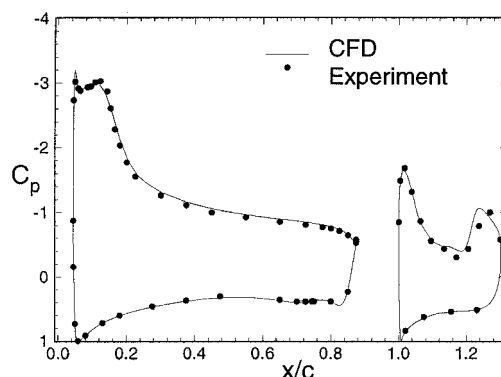

Fig. 8   Vortex breakdown structure.

Fig. 9   Chordwise pressure distribution over two-element EET model ($\delta_f = 30$ deg, $M = 0.2$, and $Re = 7.2 \times 10^6$).

extent of the breakdown region, the location of the stagnation point, and the dividing streamlines. The breakdown area is roughly circular with a two-cell internal structure. The axial velocity in the vortex core reaches nearly twice the freestream velocity ahead of the stagnation point. On the other hand, the reversed flow magnitude inside the breakdown region is limited to 40% of the freestream speed.

For the second case studied, the flap deflection was increased to 30 deg while keeping all other parameters fixed. The chordwise C_p distribution at a spanwise location of 1 in. from the flap side edge is given in Fig. 9. The agreement between measured values and computed results is excellent. A comparison with PSP measurements also showed remarkable agreement as in case 1. In general, the side-edge flowfield at this higher flap-deflection angle is very similar to the preceding case ($\delta_f = 20$ deg) described in detail. Therefore, it is sufficient to highlight only the significant differences between the two cases.

The first major difference between cases 1 and 2 involves the strength of the spanwise jetting through the side-lap region. Owing to the larger opening between the wing and the flap surfaces, the spanwise flow in case 2 is relatively weaker, and its effect on the top flap vortex is accordingly smaller. Second, because of the higher flap loading in case 2, the two flap vortices are stronger than those in case 1. However, in both cases the dual vortex system is dominated by the top vortex. The streamwise velocity in the core of the top vortex attains magnitudes more than twice the freestream value compared to slower flow in case 1. Third, because of the higher adverse
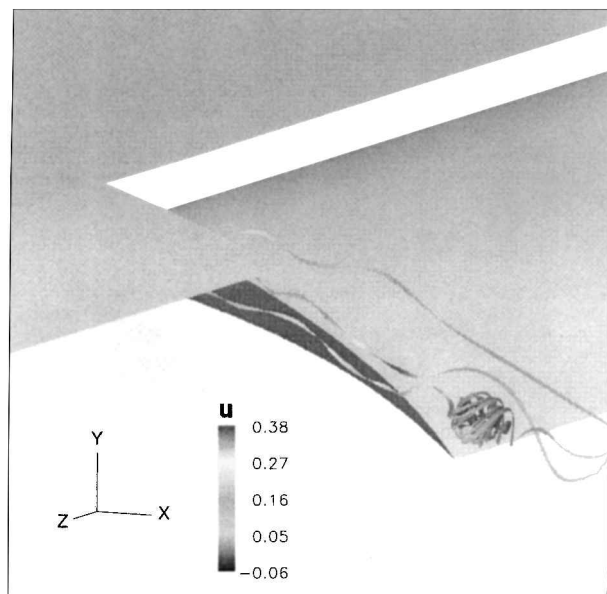

Fig. 7   Flow streamlines at flap side edge.

pressure gradient on the upper flap surface, the vortex breakdown location moves upstream and grows noticeably in size.

B. Three-Element Configuration

In case 3 the wing angle of attack is 10 deg, and the slat and the flap are deflected at 30 deg relative to the wing. The freestream conditions are the same as those in the preceding simulations. Figure 10 shows the chordwise C_p variation for the three elements at a distance of 1 in. (0.046 cm) from the flap side edge. Uncertainty in the surface-pressure experimental data is also included in Fig. 10 with error bars. Excellent repeatability of the surface pressures was observed during the experiments. Note that the large uncertainty of ± 0.13 in slat upper surface-pressure coefficients stems from the electronic scanning pressure module size generally used in this region for high-lift testing.

Once again the agreement is excellent between measured and computed values of surface pressure. A comparison between Figs. 9 and 10 shows that the presence of the slat does not significantly alter the flowfield around the flap. The main influence of the slat is to accelerate the flow over the upper surface of the wing, i.e., to increase the suction peak.

The Mach contours in Fig. 11 indicate three different regions of flow separation (depicted by dark areas of low-Mach-number flow) that can sustain significant flow unsteadiness and, hence, are likely to be important contributors to the overall airframe noise. The first
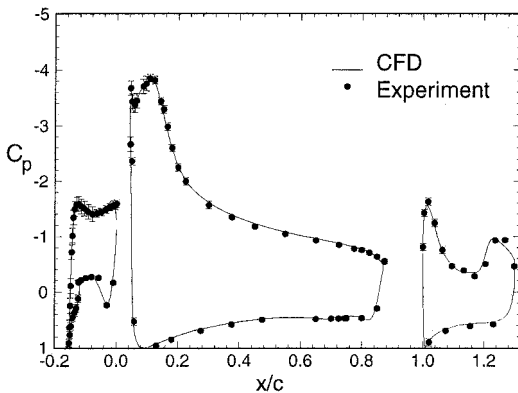

Fig. 10 Chordwise pressure distribution over three-element EET model (δ_s = 30 deg, δ_f = 30 deg, M = 0.2, and Re = 7.2 × 10^6).
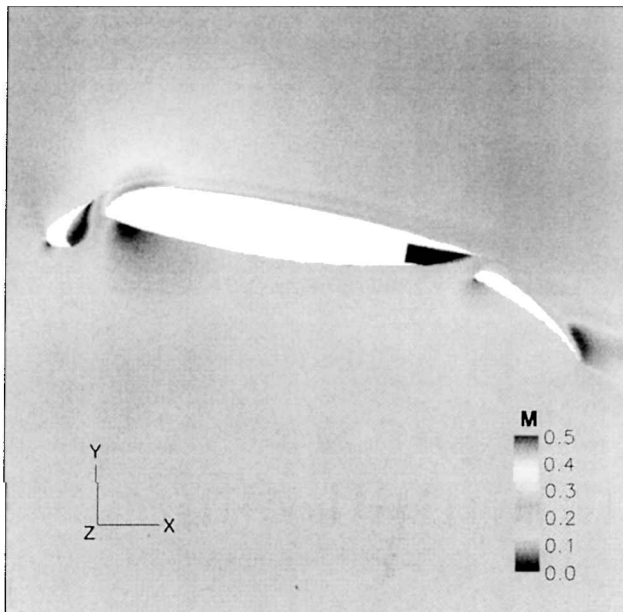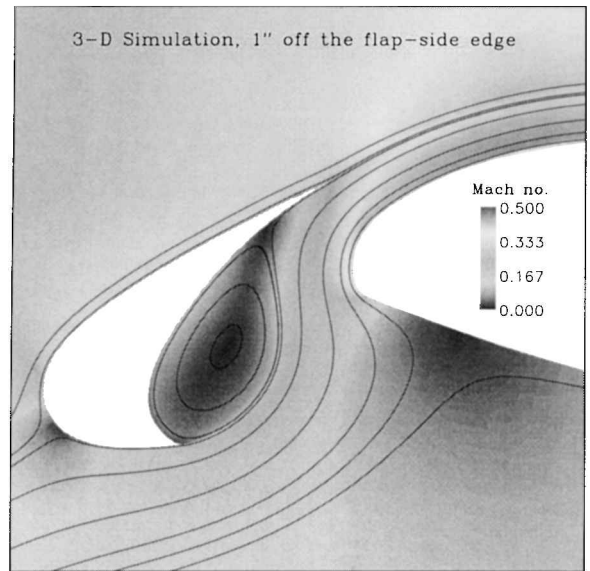

Fig. 11 Mach contours.

Fig. 12 Slat cove region flow.

region involves the recirculating zone in the slat cove. Here, the slat boundary layer separates at the cusp and forms a strong free shear layer. This shear layer, which reattaches on the slat's bottom surface near the trailing edge, forms the dividing streamlines between the recirculating zone and the flow through the gap. A similar development establishes the second region of flow separation in the main-element cove region. The third region of slow moving fluid is situated on the flap top surface near the side edge and is associated with the breakdown of the flap top vortex. The flap side-edge flowfield and vortex breakdown process follows the exact pattern described in detail for the two-element configuration and therefore will not be discussed again. The flow visualizations and comparison of surface-pressure variations over the trailing-edge portion of the main wing and flap indicated no change because of the addition of a slat.

The confluent boundary layer in the wake of the slat is clearly seen in the Mach contours displayed in Fig. 11. Similar confluent boundary layers have been observed in other experiments involving high-lift configurations.[16,17] This turbulent confluent boundary layer may also have a role in the noise generation process. To ensure proper resolution of the confluent region, the computational grid was designed to include a significant number of points in the slat wake over the top of the main element.

The details of the slat cove flowfield in a spanwise plane are shown in Fig. 12. In this figure the streamlines are added to Mach contours to augment understanding of the flow physics. The slat cove flowfield was found to be essentially two-dimensional; the flow showed insignificant spanwise dependence. A significant amount of air is trapped in the slat cove forming a low-speed recirculating flow. A free shear layer also develops between this low-speed recirculating zone and the faster flow forced through the gap between the main wing and the slat. This shear layer emanates from the cusp of the slat and is captured all the way up to the lower slat surface, where the flow reattaches on the lower surface near the trailing edge. On the faster side of the free shear layer, the fluid particles are accelerated through the gap between the shear layer and the wing surface, reaching speeds as high as two and one-half times the freestream.

IV. Conclusions

This research has demonstrated the utility of the RANS framework toward identification and understanding of the complex airframe noise sources associated with realistic, high-Reynolds-number, high-lift flowfields. A comparison of the EET flowfield with the previously computed solution for the QFF and 7 × 10 tunnel test configurations[8] shows that the details of acoustically relevant flow features near a flap side edge can depend significantly on

the specific geometry of the high-lift configuration. In particular, it was found that unlike the QFF and 7×10 cases the post merger flap side-edge vortex on the EET flap remains in close proximity to the flap upper surface. The resulting interaction with the flap trailing edge may contribute significantly to the acoustic field. In addition, the unsteadiness sustained by the strong spanwise jetting across the significantly large side-lap region may also contribute a visible signature to the measured acoustic spectrum. A preliminary analysis of the measured acoustic data appears to support the preceding conjectures. However, for a more definitive confirmation one must await detailed unsteady simulations accompanied by prediction of acoustic radiation. Studies of this nature are currently underway.

Important slat flow features, such as the confluent boundary layer, the free shear layer and the slat wake, were also captured. Similar to the physical mechanisms of flap noise, the preceding features determine the frequency spectrum and amplitude of the local flow unsteadiness, which eventually generates the far-field noise, either by itself or via interactions with the neighboring solid surfaces.

Follow-up research currently underway involves time-accurate RANS simulation of the high-lift EET wing flow. The unsteady vortex shedding from the blunt slat trailing edge was recently simulated over a two-dimensional domain with a highly concentrated grid in the slat cove region. Finally, steady RANS simulations will be extended to the next building-block configuration, which involves a swept, tapered wing with two flap side edges that is currently being tested at NASA Langley.

Acknowledgments

References

[1]Crighton, C. R., "Airframe Noise," *Aeroacoustics of Flight Vehicles: Theory and Practice*, Vol. 1: Noise Sources, NASA TR-90-3052, 1991, pp. 391–447.

[2]Macaraeg, M. G., "Fundamental Investigations of Airframe Noise," AIAA Paper 98-2224, June 1998.

[3]Dobrzynski, W., Nagakura, K., Gehlhar, B., and Buschbaum, A., "Airframe Noise Studies on Wings with Deployed High-Lift Devices," AIAA Paper 98-2337, June 1998.

[4]Fink, M. R., "Noise Component Method for Airframe Noise," *Journal of Aircraft*, Vol. 16, No. 10, 1979, pp. 659–665.

[5]Storms, B. L., Takahashi, T. T., and Ross, J. C., "Aerodynamic Influence of a Finite-Span Flap on a Simple Wing," Society of Automotive Engineers, Paper 951977, Sept. 1995.

[6]Radeztsky, R. H., Singer, B. A., and Khorrami, M. R., "Detailed Measurements of a Flap Side-Edge Flow Field," AIAA Paper 98-0700, Jan. 1998.

[7]Khorrami, M. R., Singer, B. A., and Takallu, M. A., "Analysis of Flap Side-Edge Flowfield for Identification and Modeling of Possible Noise Sources," Society of Automotive Engineers, Paper 971917, May 1997.

[8]Khorrami, M. R., Singer, B. A., and Radeztsky, R. H., Jr., "Reynolds Averaged Navier–Stokes Computations of a Flap Side-Edge Flow Field," *AIAA Journal*, Vol. 37, No. 1, 1999, pp. 14–22.

[9]Takallu, M. A., and Laflin, K. R., "Reynolds-Averaged Navier–Stokes Simulations of Two Partial-Span Flap Wing Experiments," AIAA Paper 98-0701, Jan. 1998.

[10]Mathias, D. L., Roth, K. R., Ross, J. C., Rogers, S. E., and Cummings, R. M., "Navier–Stokes Analysis of the Flow About a Flap Edge," *Journal of Aircraft*, Vol. 35, No. 6, 1998, pp. 833–838.

[11]Khorrami, M. R., and Singer, B. A., "Stability Analysis for Noise-Source Modeling of a Part-Span Flap," AIAA Paper 98-2225, June 1998.

[12]Streett, C. L., "Numerical Simulation of Fluctuations Leading to Noise in a Flap-Edge Flowfield," AIAA Paper 98-0628, Jan. 1998.

[13]Lin, J. C., and Dominik, C. J., "Optimization of an Advanced Design Three-Element Airfoil at High Reynolds Numbers," AIAA Paper 95-1858, June 1995.

[14]Thomas, J., Krist, S., and Anderson, W., "Navier-Stokes Computations of Vortical Flows over Low Aspect-Ratio Wings," *AIAA Journal*, Vol. 28, No. 2, 1990, pp. 205–212.

[15]Spalart, P. R., and Allmaras, S. R., "A One-Equation Turbulence Model for Aerodynamic Flows," AIAA Paper 92-0439, Jan. 1992.

[16]Thomas, F. O., Nelson, R. C., and Liu, X., "An Experimental Investigation of Unsteady Effects in a High-Lift System," AIAA Paper 98-0704, Jan. 1998.

[17]McGinley, C. B., Anders, J. B., and Spaid, F. W., "Measurements of Reynolds Stress Profiles on a High-Lift Airfoil," AIAA Paper 98-2620, June 1998.